Engineering Structures 126 (2016) 432–445

Contents lists available at ScienceDirect

Engineering Structures

journal homepage: www.elsevier.com/locate/engstruct

# Seismic performance of fiber-reinforced concrete interior beam-column joints

Xing-wen Liang *, Ying-jun Wang, Yi Tao, Ming-ke Deng

*Department of Civil Engineering, Xi'an University of Architecture and Technology, Yanta Road 13#, Xi'an 710055, China*

ARTICLE INFO

*Article history:*
Received 25 July 2014
Revised 2 August 2016
Accepted 3 August 2016
Available online 11 August 2016

*Keywords:*
Beam-column joint
Fiber-reinforced concrete
Quasi-static test
Seismic performance
Numerical simulation

ABSTRACT

Fiber-reinforced concrete (FRC), as an advanced alternative to normal concrete, has been increasingly used to construct beam-column joints which is one of the most congested parts of reinforcements in reinforced concrete (RC) structures because of its potentially beneficial properties. The present work aims to investigate the seismic performance of FRC beam-column joints experimentally and numerically. A total of eight beam-column joints, including both FRC beam-column joints and RC beam-column joint, were conducted to explore its seismically important features under quasi-static reversed cyclic load, mainly including the failure modes, hysteretic response, energy dissipation, stiffness degradation. It was found that the application of FRC can effectively improve the seismic performance of beam-column joints because it leads to higher load-carrying capacity and a greater deformation capability prior to the formation of the major diagonal cracks in the joint core zone. A numerical study, using the Open System for Earthquake Engineering Simulation (OpenSEES), was also conducted to study the seismic performance of beam-column joints deeply after its applicability and accuracy being validated with test data. The prediction from the proposed numerical model shows a good agreement with test data. Furthermore, a parametric study was generated to address and evaluate the effects on the seismic performance of FRC beam-column joints from different parameters, including the axial load ratios, transverse reinforcement ratios and FRC compressive strength. The results indicate that the increment of axial load ratios and FRC compressive strength can enhance the load-carrying capacity.



## 1. Introduction

Beam-column joints in RC frame structures under earthquake-induced lateral deformation are generally subjected to a large shear action that leads to serious damage and stiffness degradation of the structures. In order to provide a good seismic performance, the structural components, such as, beam-column joints, must possess enhanced deformation capability and damage tolerance. Several pioneers have devoted to investigate the seismic performance of RC joints under shear reversals [1–3], whose achievements have been contributed to unveil design guidance issued by some institutes [4,5]. The previous researches have shown that beam-column joints with good deformation capability in frame structures can deliver a positive contribution to the seismic performance of structures. The current Chinese design guidance, GB 50010-2010 [5], focuses on the following three aspects to secure the earthquake-resistance capacity of beam-column joints: (1) defining the minimum transverse reinforcement ratio and diameter, as well as the maximum transverse reinforcement spacing in the joint core zone; (2) limiting the dimensions of the joint core zone to associate the sizes of beam and column; and (3) specifying the anchorage of reinforcements passing through the joint core zone in terms of length and configuration. Meanwhile, a strong column-weak beam requirement needs to be satisfied.

Beam-column joints, which are usually expected to experience greater reversed cyclic action such as an earthquake, need to be properly designed to provide a sufficient deformation capability. Severe reinforcement congestion and construction difficulties thus may occur once the longitudinal reinforcements in both beams and columns are settled as well. Furthermore, it may either lead to a larger column and/or beam sections or a greater amount of smaller diameter bars being used in order to satisfy the minimum anchorage length requirements crossing the joint core zone, which could deteriorate the reinforcement congestion or construction difficulties.

The seismic design of structures has evolved towards a performance-based design method in recent years. Therefore, there

* Corresponding author.
*E-mail addresses:* liangxingwen2000@163.com (X.-w. Liang), yingzikd@126.com (Y.-j. Wang), taoyi01@gmail.com (Y. Tao), dengmingke@126.com (M.-k. Deng).

http://dx.doi.org/10.1016/j.engstruct.2016.08.001
0141-0296/

is need for new structural members and systems that possess enhanced deformation capability and damage tolerance without complex reinforcement arrangements. The development of highly damage-tolerant beam-column joints would allow moderate shear distortions in the joint core zone, reduce rotation demands in plastic hinge zone of beam ends, and avoid seismic strengthening of the joint core zone. One option for achieving this goal is to use FRC [6,7] to upgrade the deformation capability of beam-column joints. Experimental studies [8,9] have proved that an improved seismic performance can be achieved, in terms of the shear-critical members such as beam-column joints, squat walls, coupling beams, and flexural members subjected to high shear stress by using FRC.

The objective of this study is to verify the feasibility of FRC as a replacement of normal concrete used in the joint core zone, adjacent beam end and column end, to increase stirrup spacing, reduce steel reinforcement congestion as well as construction difficulty of the joint core zone without reduction of load-carrying capacity and deformation capability by the usage of FRC, to study the influence of axial load ratios of column top on the general performance of FRC specimens, and to verify the numerical simulation results by experimental data and produce a comprehensive parametric study by using OpenSEES [10]. The present work builds upon the limited earlier work in the literatures to investigate the contribution of FRC material in enhancing the seismic performance of beam-column joints during earthquake excitation and to analyze the parameters influencing the seismic performance of FRC beam-column joints.

## 2. Research objectives and significance

Under seismic actions, the joint core zone is in tension on one diagonal direction of the joint and compression on other diagonal direction, so the joint core zone easily happens to shear failure, which causes collapse of whole structure. By the usage of FRC, the seismic performance of whole structure can be improved.

The main objective of this research is to investigate the structural behavior of beam-column joints by substituting normal concrete with FRC in the joint core zone, adjacent beam end and column end, and reducing the amount of transverse reinforcements in the joint core zone, to investigate the influence of axial load ratio of column top on the structural behavior, as well as to analyze the influence of main parameters on the structural behavior of FRC beam-column joints by numerical simulation. The study aims to improve seismic performance of FRC beam-column joints, including load-carrying capacity, energy absorption capacity and stiffness degradation.

The outcome of this study would be helpful to support the ongoing theory calculation model study of FRC beam-column joints [11,12] and their effective use in structural applications. It will be particularly helpful to make use of local materials to prepare FRC, improve seismic performance of structures, reduce property loss and secure the safety of life.

## 3. Review of related literatures

During the past 40 years, a limited number of researches [13–25] have been conducted to verify whether normal concrete can be substituted with FRC in the joint core zone, plastic hinge zone of beam end and column end, and the transverse reinforcements of the joint core zone can be reduced without reduction of load-carrying capacity and deformation capability. A brief overview of the study done and the main results reported in four of the most relevant studies are as follows.

In 1977, Henager [13] conducted FRC beam-column joints to reduce reinforcement congestion of the joint core zone. Experimental results indicate that the damage tolerance and crack resistant of FRC beam-column joints is better than that of RC beam-column joints.

In 1994, Filiatrault et al. [14] conducted four full-scale exterior beam-column joints with steel fiber reinforced concrete in the joint core zone. Experimental results indicate that steel fiber reinforced concrete is a promising material to substitute conventional confining reinforcements, the joint shear strength by the usage of steel fiber can be improved and the transverse reinforcements of the joint core zone can be reduced.

In 2005, Parra-Montesinos et al. [15] conducted two approximately 3/4 scale high-performance fiber-reinforced cement composites (HPFRCCs) beam-column joints with a small axial load corresponding to approximate 4.0% of the column axial load capacity and without transverse reinforcement in the joint core zone to evaluate the adequacy of the proposed joint design for use in zones of high seismicity. HPFRCC material was used in the joint core zone and adjacent beam regions over a length equal to twice the beam depth. Experimental results indicate that HPFRCC beam-column joints have excellent damage tolerance under large shear reversals, deformation capability, and bond capacity between beam longitudinal reinforcement and surrounding HPFRCC material even though the joint design did not satisfy minimum anchorage length requirements specified in the ACI Building Code. In addition, the ACI joint shear stress limit of $5/4\sqrt{f'_c}$ (MPa) can be also safely used in HPFRCC joint without transverse reinforcements.

In 2014, Qudah and Maalej [16] conducted nine one-third scale Engineered Cementitious Composites (ECC) beam-column joints, with different transverse reinforcement spacing and arrangement in the plastic hinge zone of beam end, column end, and/or joint core zone and without axial load on the top of column to evaluate the feasibility of enhancing performance by substituting normal concrete and partial transverse reinforcements with ECC. Experimental results indicates that the usage of ECC material as a replacement of normal concrete and partial replacement of transverse reinforcements can significantly enhance shear resistance, energy absorption capacity and cracking response, and reduce reinforcement congestion and construction complexity of the joint core zone.

In summary, the results of these studies are encouraging. However, a large amount of experimental evidences are required before the reasonable calculation model of FRC beam-column joint is determined and these proposed special designs can be applied in practical projects widely.

## 4. Experimental program

### 4.1. Description of specimens

In the present study, a total of eight 1/2 scale beam-column joints, namely, FRCJ1–FRCJ7 representing FRC specimens and RCJ1 representing RC specimen, were constructed and tested. In terms of FRC specimens, FRCJ1 was the control specimen and the others were constructed with representative characteristics. Specimen RCJ1 was casted using normal concrete for comparison.

Fig. 1 illustrates detailing of geometry and reinforcement configuration in the beam-column joints. Ends of columns and beams were points of contra-flexure. All columns have a cross section of 250 × 250 mm with a total height of 2000 mm and the transverse beam has a cross section of 150 × 300 mm with a total length of 2650 mm. Longitudinal reinforcements in the columns consisted of 4⌀16 bars (a diameter of 16 mm and the grade HRB400 steel), and those for beams consisted of 3⌀16 bars top bars and 3⌀16 bottom bars. Transverse reinforcements in columns, beams and joint core zone consisted of 6 mm-diameter reinforcement.

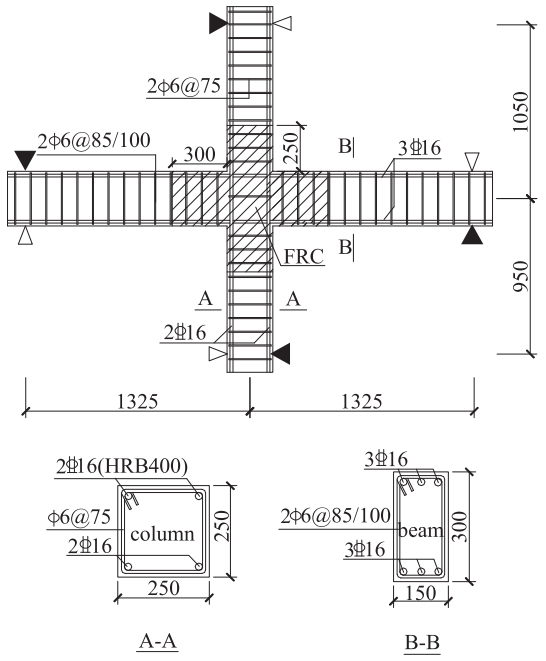


**Fig. 1.** Geometry and reinforcement configuration of specimens (except for RCJ1 where no FRC is used) (units: mm).

FRC was poured into the joint core zone, potential plastic hinge zone of beam (1.0 times of the beam depth for FRCJ1–4 and 6–7, 1.5 times of the beam depth for FRCJ5), and potential plastic hinge zone of column (1.0 times of the column depth for FRCJ1–4 and 6–7, 1.5 times of the column depth for FRCJ5). A ready-mixed normal concrete was poured into the rest of parts after 3 days for FRC curing.

### 4.2. Materials

#### 4.2.1. Production of FRC

FRC was composed of cementitious materials (mixture of 42.5R Portland Cement and fly ash), sand (maximum aggregate size < 1.18 mm), polyvinyl alcohol (PVA) fiber, water and a high-range water-reducing agent, and the mix proportion of cement: fly ash: sand: water is 1:1:0.72:0.72. The 2.0% fiber volume was optimized based on data from previous study [26] and the properties of PVA fiber from manufacturer are listed in Table 1. Different from normal concrete, PVA fibers are used to improve crack resistance and deformation capability. However, the elastic modulus of FRC is usually lower than that of normal concrete due to the absence of coarse aggregates.

#### 4.2.2. Tensile characteristics of FRC

The tensile behavior of FRC, as one of the most important characteristics, was investigated by employing the uniaxial tensile method in this study. As shown in Fig. 2(a), the dimension at fixed ends of each specimen is 80 mm × 80 mm × 16 mm (length × width × depth), and the measured dimension in the middle part of each specimen is 160 mm × 50 mm × 16 mm (length × width × depth). One linear transformer (LVDT), which was parallel to the loading direction, was fixed at the upper and lower ends of the measured region for each specimen to measure the axial tensile deformation, and the loading rate was 0.1 mm/min.

**Table 1**
Performance indicators of PVA fiber.

| Property | Value |
|---|---|
| Fiber length | 12 mm |
| Diameter | 39 μm |
| Tensile strength | 1600 MPa |
| Young's modulus | 40 GPa |
| Elongation (%) | 7 |

The uniaxial tensile stress-strain curves of FRC are plot in Fig. 2 (b), and it can be observed that its ultimate tensile strain can reach to around 0.6%, showing an evident tensile strain-hardening performance. The maximum stress obtained from the tensile stress-strain curve of FRC is defined as the tensile strength, and its initial slop is defined as elastic modulus.

#### 4.2.3. Properties of FRC, concrete and reinforcements

In this study, the average cubic compressive strength of FRC with a dimension of 100 mm × 100 mm × 100 mm is 56.6 MPa, and its average tensile strength is 6.99 MPa with the elastic modulus of $1.71 \times 10^4$ MPa.

The cubic compressive strength of concrete with a dimension of 150 mm × 150 mm × 150 mm measured is 48 MPa with the elastic modulus of $3.41 \times 10^4$ MPa.

According to uniaxial tensile tests, the regular deformed reinforcement with a diameter of 16 mm has a yield strength of 427 MPa and ultimate strength of 609 MPa, while the round reinforcement with a diameter of 6 mm has a yield strength of 273 MPa and ultimate strength of 440 MPa.

### 4.3. Test procedure

A schematic view of the loading apparatus is shown in Fig. 3. The column was supported using a steel hinge attached to strong floor. The beam ends were supported using rollers to allow rotation and free horizontal movement. A constant axial load was gradually applied on the top of the column. To simulate seismic stimulation, a reversed cyclic horizontal load was then applied at the top end of the column through an actuator mounted on the reaction wall.

Loading-controlled scheme was used to apply the horizontal load until the longitudinal reinforcements yielded. The amplitude of load was increased by 5 kN each cycle. Yield displacement was initially determined with yielding of the longitudinal reinforcements in beams and columns. It was turned to displacement control afterwards and the amplitude of displacement was increased by 10 mm, and each level of horizontal displacement was repeated three times. The horizontal loading was gradually removed when the residual load-carrying capacity reduced to around 60% of the peak load-carrying capacity or an unstable hysteretic loop appeared.

## 5. Test results and discussion

The seismic performance of both FRC specimens and RC specimen was analyzed in the section based on their failure modes, hysteric behavior and energy dissipation ability. All eight specimens were generally divided into three groups considering the critical variables of each specimen, for example, group 1 includes FRCJ1 and RCJ1, group 2 includes FRCJ2–FRCJ5 which only exhibits the varying axial load ratios, and the last group is for FRCJ6 and FRCJ7 consisted of different transverse reinforcement ratios (see Table 2).

### 5.1. Failure modes

Fig. 4 shows the crack patterns before major diagonal cracks occurred in the joint core zone. Fig. 5 shows the pictures of the final failure modes of each specimen. Table 3 lists the load-carrying

(a) The loading apparatus of uniaxial tensile test

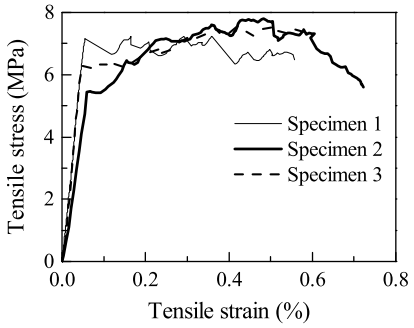


(b) The uniaxial tensile stress-strain curves

**Fig. 2.** The uniaxial tensile test and stress-strain curves of FRC.

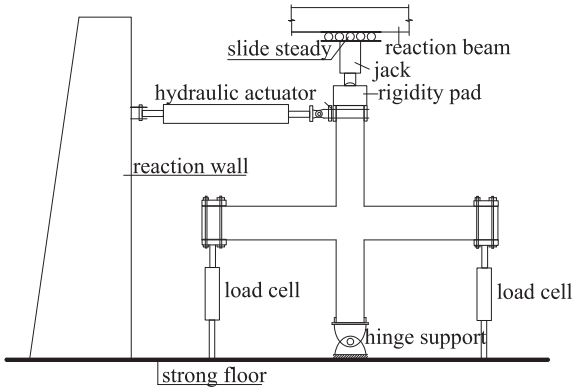


**Fig. 3.** A schematic view of the loading apparatus.

**Table 2**
Basic parameters of specimens.

| Specimens | $M$ | $f_t$ (MPa) | $E_c$ (MPa) | $n_d$ | $n_t$ | $\rho_{sv}$ (%) | $M_{c,t}/M_{b,t}$ |
|---|---|---|---|---|---|---|---|
| RCJ1 | C | 3.32 | 34,100 | 0.40 | 0.18 | 0.152 | 1.28 |
| FRCJ1 | FRC | 6.99 | 17,100 | 0.42 | 0.19 | 0.152 | 1.31 |
| FRCJ2 | FRC | 6.99 | 17,100 | 0.16 | 0.07 | 0.152 | 0.79 |
| FRCJ3 | FRC | 6.99 | 17,100 | 0.18 | 0.08 | 0.152 | 0.88 |
| FRCJ4 | FRC | 6.99 | 17,100 | 0.48 | 0.22 | 0.152 | 1.44 |
| FRCJ5 | FRC | 6.99 | 17,100 | 0.60 | 0.27 | 0.152 | 1.60 |
| FRCJ6 | FRC | 6.99 | 17,100 | 0.42 | 0.19 | 0.228 | 1.31 |
| FRCJ7 | FRC | 6.99 | 17,100 | 0.42 | 0.19 | 0.380 | 1.31 |

*Note:* $M$ represents the matrix materials; C represents the normal concrete; $f_t$ represents the uniaxial tensile strength; $n_d$ and $n_t$ represents the design and test axial load ratios, respectively; $\rho_{sv}$ represents transverse reinforcement ratios in joint core zone; $M_{c,t}$ and $M_{b,t}$ represent the flexure strength of column end and beam end.

capacity and lateral drift when the major diagonal crack nearly occurred in the joint core zone.

*5.1.1. Specimens RCJ1 and FRCJ1*

For the specimen RCJ1, a few flexural cracks occurred in the beams at a drift of 0.3%. With the drift increasing to 0.75%, the first diagonal crack eventually formed in the joint core zone. After the formation of major diagonal cracks in the joint core zone (Fig. 4a), there was no further propagation of cracks in beams and columns. When the drift of 1.23% was achieved, the diagonal cracks extended into the columns. Once the drift increased to 2.63%, the major diagonal crack in the joint core zone widened suddenly and was accompanied by a significant spalling of concrete cover. Only the joint core zone furtherly damaged with the growing of drift. As observed from the final failure mode (Fig. 5a), there were only a few diagonal cracks occurred through the loading history. Failure of the RCJ1 was due to shear in the joint core zone.

For the control specimen FRCJ1, multiple flexural cracks and shear cracks occurred in beams at a drift of 0.44%. With the drift increasing to 0.69%, the first diagonal crack eventually formed in the joint core zone. After the formation of major diagonal cracks in the joint core zone (Fig. 4b) at a drift of 2.33%, there was no further propagation of cracks in beams and columns. These diagonal cracks expanded and widened gradually as the drift continuously increased. Once the drift of 4.59% was attained, the diagonal cracks extended into columns. As the drift continuously increased, the diagonal cracks connected together in the joint core zone (Fig. 5b). It is noticed that there was no spalling of FRC cover occurred in the joint core zone accompanied by opening or closing of cracks, and eventually FRCJ1 failed in shear in the joint core zone accompanied by the yielding of the longitudinal reinforcements in beams.

*5.1.2. Specimens FRCJ2–FRCJ5*

The overall behavior of FRCJ2–FRCJ5 was similar to that of the control specimen (FRCJ1). Firstly, multiple fine cracks initiated from beams. New cracks appeared and developed slowly, and there was no significant widening of formed cracks. Secondly, first diagonal crack appeared in the joint core zone. As the drift progressively increased, although many parallel micro cracks appeared along the first diagonal crack, there was no visible increase in the width of cracks. Thereafter, major diagonal cracks grew and widened suddenly in the joint core zone (Fig. 4c–f). Meanwhile, there was no further growing of cracks in beams and columns except for both FRCJ2 and FRCJ3 in which horizontal cracks were observed in columns, this is due to the yield of column longitudinal reinforcements of FRCJ2 and FRCJ3, for which flexural strength ratio of column to beam (shown in Table 2) is <1. Finally, further damage was observed in the joint core zone and consequently

**Table 3**
The load-carrying capacity and lateral drift when the major diagonal crack nearly occurred in the joint core zone.

| Specimens | RCJ1 | FRCJ1 | FRCJ2 | FRCJ3 | FRCJ4 | FRCJ5 | FRCJ6 | FRCJ7 |
|---|---|---|---|---|---|---|---|---|
| $V$ (kN) | 62.35 | 80.57 | 64.25 | 69.18 | 78.52 | 84.75 | 69.95 | 72.83 |
| $\theta$ (%) | 1.16 | 2.33 | 2.44 | 2.70 | 2.78 | 1.79 | 2.86 | 3.03 |

*Note:* $V$ represents the load-carrying capacity; $\theta$ represents the lateral drift of column top.

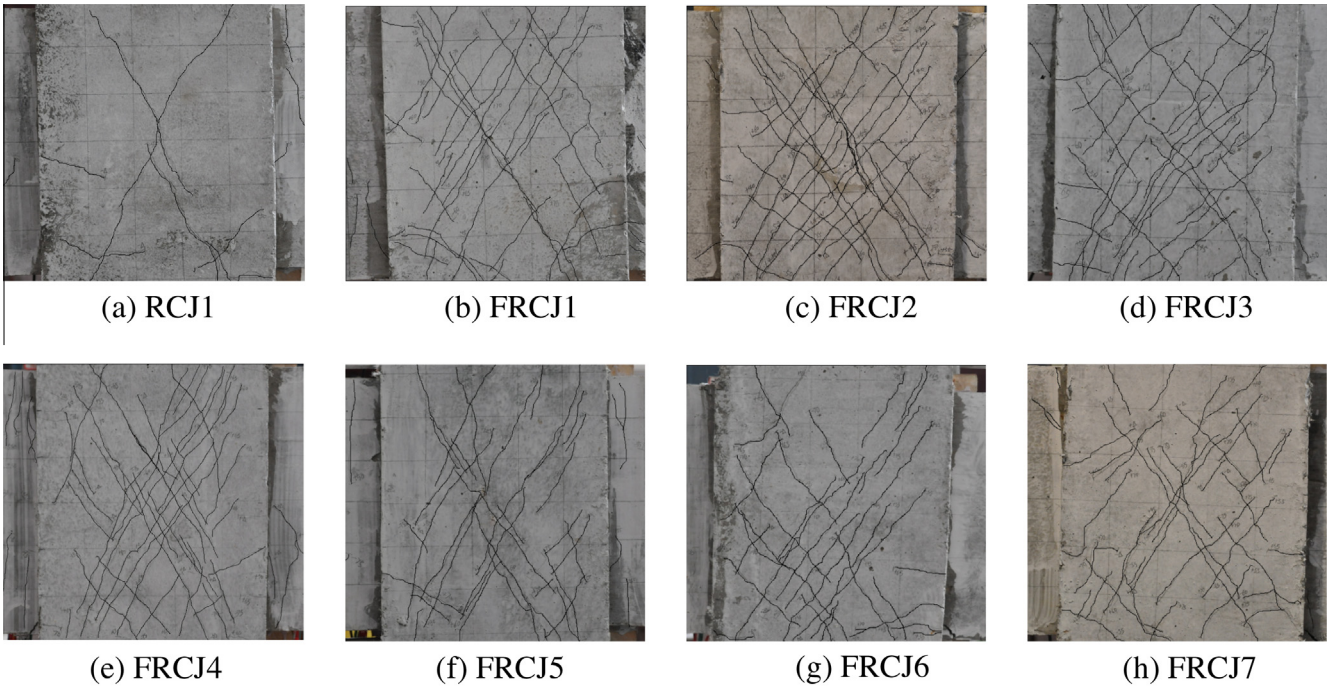


**Fig. 4.** Crack patterns before major diagonal cracks occurred in the joint core zone.

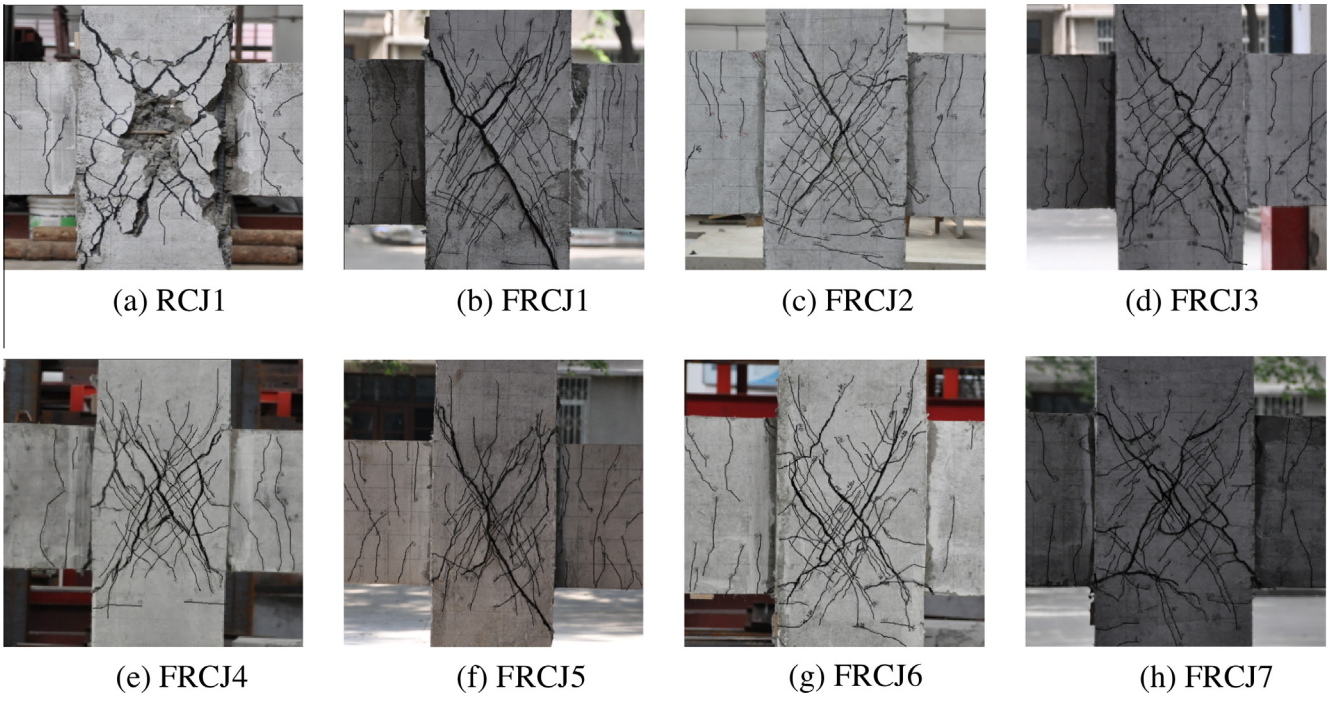


**Fig. 5.** Final failure modes of specimens.

resulted in the failure of beam-column joints. It is noticed that there was no spalling of FRC cover in the joint core zone accompanied by opening or closing of cracks (Fig. 5c–f). Failure of both FRCJ2 and FRCJ3 was caused by a combination of shear failure of the joint core zone and yielding of longitudinal reinforcements in columns. In contrast, both FRCJ4 and FRCJ5 failed due to a combination of shear failure of the joint core zone and yielding of longitudinal reinforcements in beams.

*5.1.3. Specimens FRCJ6 and FRCJ7*

The overall behavior of both FRCJ6 and FRCJ7 was also similar to that of the control specimen FRCJ1. Multiple flexural cracks were initially observed in the beams at a drift of 0.42% for FRCJ6 and 0.44% for FRCJ7, respectively. With the drift increasing to 0.76% for FRCJ6 and 0.61% for FRCJ7, diagonal cracks were eventually appeared in the joint core zone. Once the drift of 2.86% for FRCJ6 and 3.03% for FRCJ7 were attained, major diagonal cracks widened

suddenly in the joint core zone (Fig. 4g and h) and there is no further growing of cracks in beams. With the drift continuously increasing, further damage was only observed in the joint core zone even though the transverse reinforcement ratios are different, that is because bridging effect of PVA fiber in FRC makes the cracks uniform distribution and limits the development of crack width. Therefore, the increase in transverse reinforcement ratios has a small influence on the damage. It is visibly that the failure of both FRCJ6 (Fig. 5g) and FRCJ7 (Fig. 5h) were caused by a combination of shear failure of the joint core zone and yielding of longitudinal reinforcements in beams.

### 5.2. Hysteric behavior and skeleton curves

Fig. 6 shows hysteric loops from the upper column corresponding to each specimen and Fig. 7 comprises the skeleton curves of each specimen. Five feature points (marked as 1–5 in Fig. 6) were chosen from the skeleton curves under both pushing and pulling actions to investigate the load-carrying capacity and deformation capability of each specimen. Point 1 represented the crack load point when the first diagonal crack appeared in the joint core zone. Point 2 stated the yield load point determined by the yield moment method [27]. Point 3 corresponded to the peak load point and point 4 located at the ultimate load point corresponding to 85% of the peak load value, while point 5 was assigned at the collapse load point representing the last cycle in the test. The following conclusions can be drawn from Figs. 6 and 7. The mean value was adopted to process the following analysis by averaging the absolute values extracted from both pushing and pulling actions.

#### 5.2.1. Specimens RCJ1 and FRCJ1

The load-carrying capacity (point 3) and the corresponding lateral displacement of FRCJ1 are 1.19 and 1.27 times greater than those from RCJ1, respectively (Fig. 7a). This can be essentially attributed to the enhancements of shear resistance and tensile strength of the joint core zone due to the application of FRC. Comparing the hysteretic behavior between RCJ1 (Fig. 6a) and FRCJ1 (Fig. 6b), it is shown that FRC can effectively improve the shear strength and deformation capability of the beam-column joint. Also, a fatter hysteretic loop is observed from FRCJ1 compared to RCJ1, which states a greater energy dissipation capacity. The ultimate drift (point 4) of FRCJ1 is 1.33 times larger than that of RCJ1 (Fig. 7a) verifying an outstanding deformation capability of FRC specimen.

#### 5.2.2. Specimens FRCJ2–FRCJ5

The load-carrying capacity (point 3) of FRCJ3, FRCJ4 and FRCJ5 are 1.11, 1.26 and 1.34 times that of FRCJ2, while corresponding lateral displacement are 0.89, 0.87 and 0.82 times that of FRCJ2, respectively (Fig. 7b). Among the axial load ratios in this paper, the load-carrying capacity increases while the deformation capability decreases with an increase of axial load ratios. Therefore, it can be seen clearly that the greater axial load ratio leads to an increment of load-carrying capacity and a lower deformation capability, and the increment of axial load ratios performs fatter hysteric loops and a less pinched loops from Fig. 6(c–f).

#### 5.2.3. Specimens FRCJ6 and FRCJ7

Comparing the skeleton curves plotted in Fig. 7c, the load-carrying capacity (point 3) of both FRCJ6 and FRCJ7 was 0.94 and 0.97 times that from FRCJ1, but the corresponding lateral displacement was 1.00 and 1.05 times that from FRCJ1. Due to the high shear strength of FRC, the increase of the transverse reinforcements in the joint core zone has a negligible effect on load-carrying capacity. In addition, the collapse lateral displacement (point 5) of both FRCJ6 and FRCJ7 was 1.02 and 1.15 times greater than that from FRCJ1. In the late loading, the width of cracks increased furtherly, PVA fiber in FRC was snapped or pulled out, and the transverse reinforcements came into play, so the deformation capability can be largely promoted. Meanwhile, it can be also found from Fig. 7c that the increase of the transverse reinforcement ratios in the joint core zone can decelerate the degradation of the load-carrying capacity.

In summary, the pinching effect of hysteresis hoops indicates low energy dissipation. There are two reasons to explain the pinching effect: the first one is that the shear failure occurred in the joint core zone of all specimens, and the second one is that the failure modes of FRCJ2–FRCJ5 transform from flexure failure of columns to flexure failure of beams with an increase of flexural strength ratio of column to beam (shown in Table 2), so the area of hysteresis hoops increase gradually, and the pinching effect can be remitted.

### 5.3. Energy dissipation

Energy dissipation at each cycle was computed from the summation of the area enclosed by a single hysteric loop. Cumulative energy dissipation was calculated as the summation of the energy dissipated before the current hysteric loop. Fig. 8 shows the relationship between the cumulative energy dissipation and drift of each specimen corresponding to the aforementioned five feature points plotted in Fig. 6.

It can be seen from Fig. 8a that the FRCJ1 shows greater energy dissipation capacity than RCJ1. Cumulative energy dissipated by FRCJ1 at the yield load point (point 2), the peak load point (point 3), the ultimate load point (point 4) and the collapse load point (point 5) respectively were 1.48, 1.51, 2.01 and 2.33 times greater than those of RCJ1, indicating that presence of FRC can significantly improve the energy dissipation capacity of beam-column joints. It can be found from Fig. 8b that the increase of axial load ratios, such as FRCJ2–FRCJ5, resulted in a greater energy dissipation capacity of specimens. From Fig. 8 a it can be visibly seen that the cumulative

**Table 4**
Concrete mechanical properties adopted in Concrete 02.

| Specimen | C/FRC | $f_{cu}$ (MPa) | $\varepsilon_c$ | $f_{pcu}$ (MPa) | $\varepsilon_{epscu}$ | $r$ | $f_t$ (MPa) | $E_{ts}$ (MPa) |
|---|---|---|---|---|---|---|---|---|
| RCJ1 | Unconfined | 48.00 | 0.0028 | 0 | 0.0040 | 0.1 | 3.32 | 4262.5 |
| | Confined | 49.68 | 0.0031 | 9.6 | 0.0090 | 0.1 | 3.32 | 4262.5 |
| FRCJ1–FRCJ5 | Unconfined | 56.60 | 0.0066 | 0 | 0.0113 | 0.1 | 6.99 | 2137.5 |
| | Confined | 57.27 | 0.0073 | 13.30 | 0.0114 | 0.1 | 6.99 | 2137.5 |
| FRCJ6 | Unconfined | 56.60 | 0.0066 | 0 | 0.0113 | 0.1 | 6.99 | 2137.5 |
| | Confined | 57.60 | 0.0076 | 13.30 | 0.0115 | 0.1 | 6.99 | 2137.5 |
| FRCJ7 | Unconfined | 56.60 | 0.0066 | 0 | 0.0113 | 0.1 | 6.99 | 2137.5 |
| | Confined | 57.93 | 0.0079 | 13.30 | 0.0116 | 0.1 | 6.99 | 2137.5 |

*Note:* C represents the normal concrete; $r$ is the ratio between unloading slope at crushing strain and initial slop.

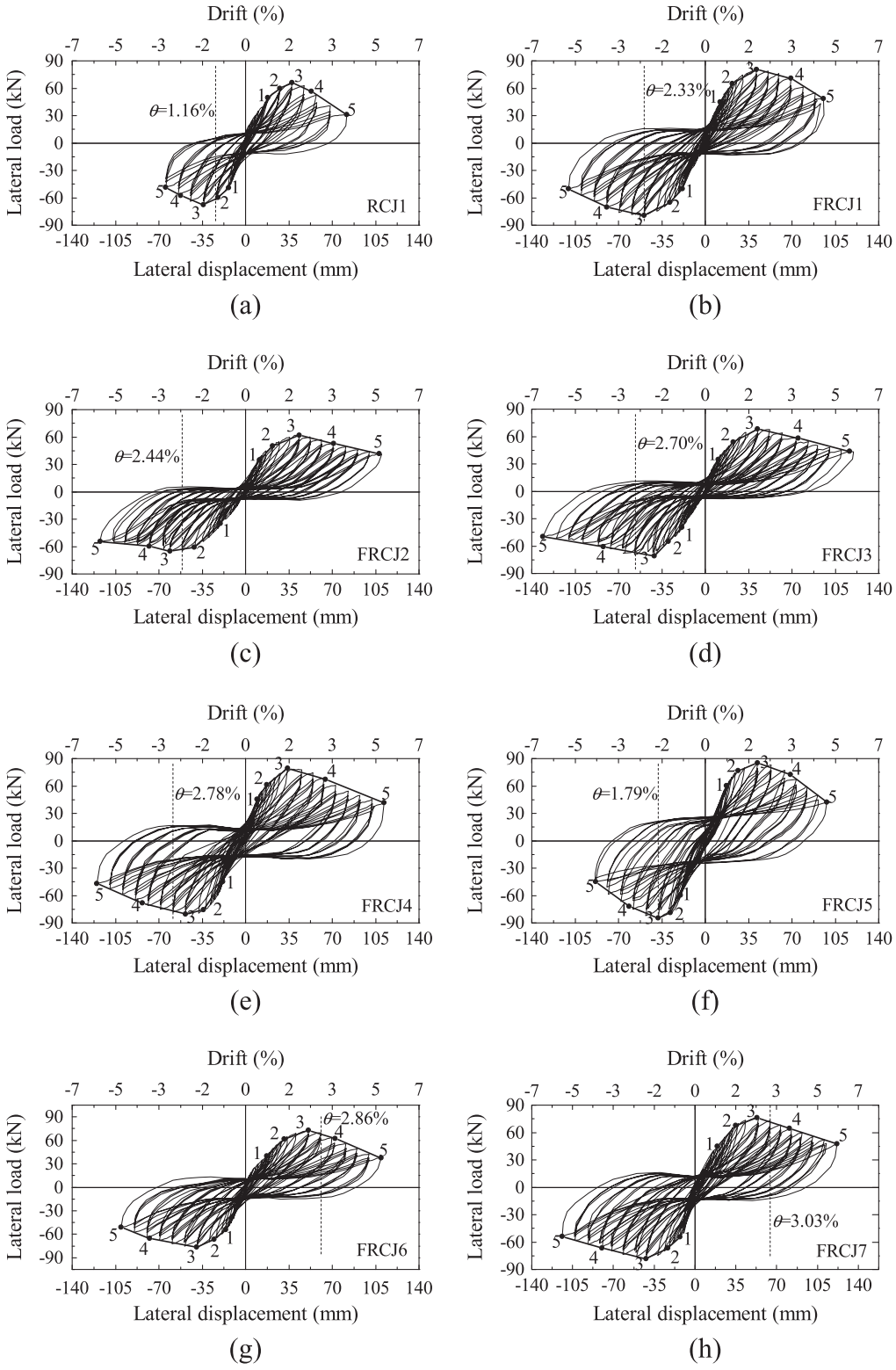


**Fig. 6.** Hysteretic curves and feature points of specimens.

energy dissipated by FRCJ7 at the five feature points were 1.45, 1.30, 1.22, 1.50 and 1.33 times greater than those absorbed by FRCJ6, and 1.11, 1.10, 1.11, 1.04 and 1.17 times greater than those absorbed by FRCJ1, respectively. It proves that the greater transverse reinforcement ratio leads to an enhanced energy dissipation capacity.

### 5.4. Stiffness degradation

Stiffness degradation from each hysteric loop was evaluated using secant stiffness which was calculated using Eq. (1) introduced in the specification for seismic test method (JGJ/T 101-2015) [28].

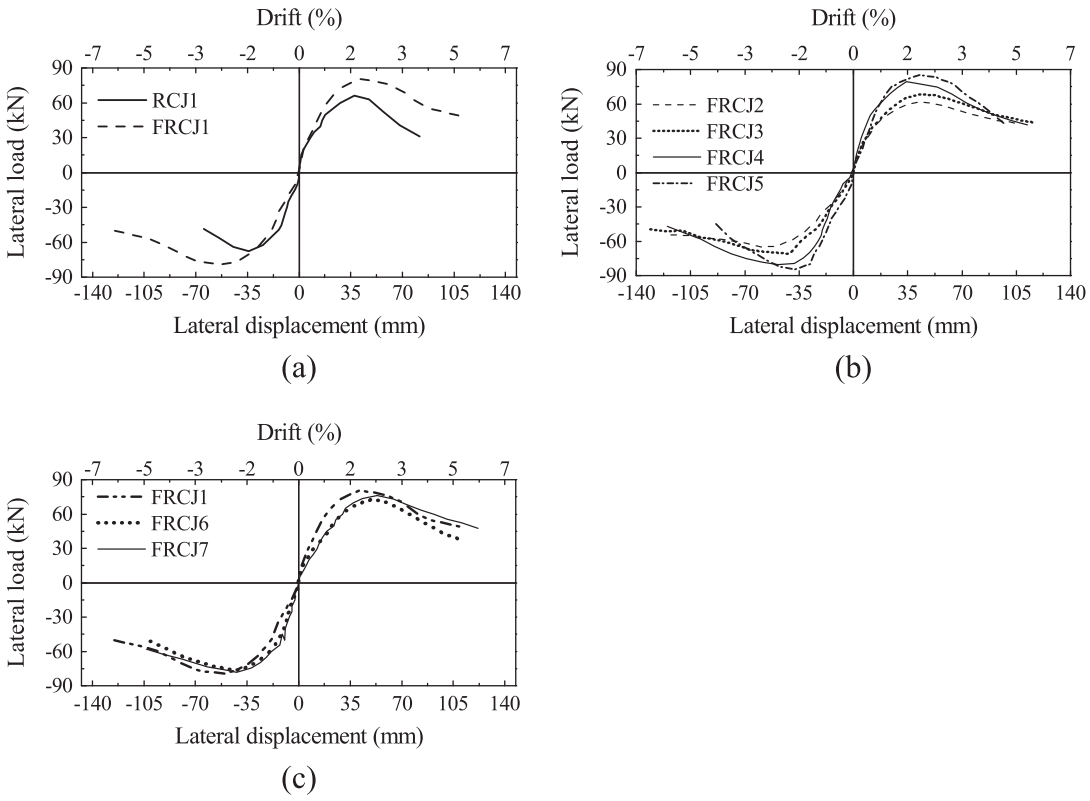


**Fig. 7.** Skeleton curves of specimens.

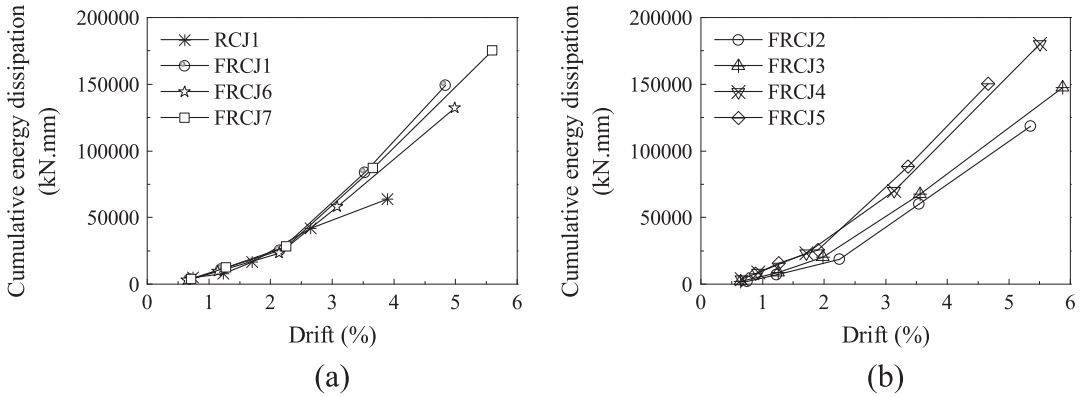


**Fig. 8.** Relationship between cumulative energy dissipation and drift.

$$K_i = (|+P_i| + |-P_i|)/(|+\Delta_i| + |-\Delta_i|) \quad (1)$$

where $K_i$ is the secant stiffness of specimen at $i$th cycle; $+P_i$ and $-P_i$ are lateral pushing and pulling actions at $i$th cycle respectively; $+\Delta_i$ and $-\Delta_i$ are the corresponding lateral displacement at $i$th cycle, respectively. Fig. 9 shows the relationship between stiffness degradation and drift of each specimen. The following conclusions can be drawn.

*5.4.1. Specimens RCJ1 and FRCJ1*

It is obviously that the initial secant stiffness of RCJ1 was 2.2 times greater than that of FRCJ1 as shown in Fig. 9a. On the contrary, the collapse drift of FRCJ1 (point 5) was 1.55 times greater than that of RCJ1. This may be attributed to the absent of coarse aggregates in FRC. However, the stiffness degradation rate of FRCJ1 was smaller than that of RCJ1. This may be contributed to the tension hardening behavior of FRC and excellent bridging ability of FRC due to the usage of PVA fibers.

*5.4.2. Specimens FRCJ2–FRCJ5*

It is shown in Fig. 9b that the initial secant stiffness of FRCJ3–FRCJ5 was 1.01, 1.42 and 1.49 times larger than that from FRCJ2 as shown in Fig. 9b. On the contrary, the collapse drift (point 5) of FRCJ3–FRCJ5 was 1.10, 1.04 and 0.83 times than that from FRCJ2. This indicates the increase of axial load ratio can enhance the initial secant stiffness, but the collapse drift (point 5) increases within the certain range of axial load ratios in this study.

*5.4.3. Specimens FRCJ6 and FRCJ7*

From Fig. 9c it is obviously that the stiffness degradation rates from these specimens were almost identical. However, the collapse drift (point 5) of both FRCJ6 and FRCJ7 was 1.01 and 1.15 times

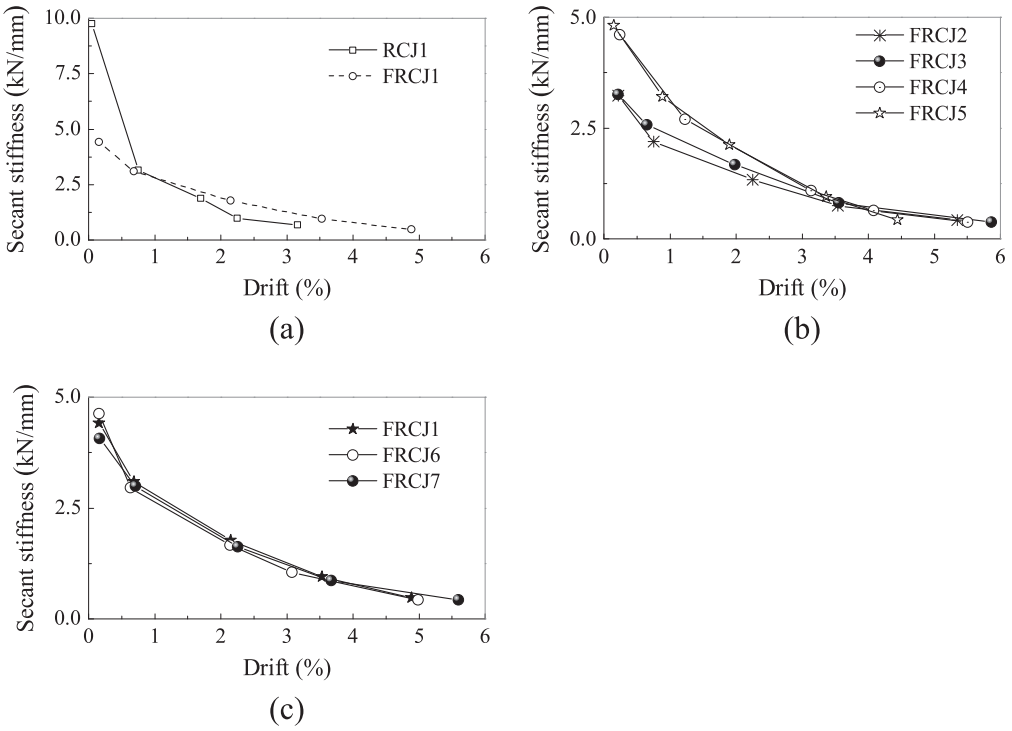


**Fig. 9.** Relationship between stiffness degradation and drift.

greater than that of FRCJ1. It reflects that the variation of the transverse reinforcement ratios of the joint core zone has limited influences on the stiffness degradation, but it can increase deformation capability.

In summary, it is visibly that the usage of FRC can dramatically improve the seismic performance of specimens in terms of cracking response, energy dissipation capacity, load-carrying capacity and deformation capability, the increasing of axial load ratios can alter failure modes, improve energy dissipation capacity and load-carrying capacity, as well as the increasing of the transverse reinforcement ratios in the joint core zone can improve energy dissipation capacity and deformation capability, reduce stiffness degradation after the peak load.

## 6. Numerical modeling

A numerical model was developed using OpenSEES [10], in which advanced formulation of fiber beam-column elements and zero-thickness nonlinear spring elements can be used to reduce the need for finer meshes with a larger number of elements and nodes that are typical of Finite Element (FE) packages. In this study, the joint core zone was represented using "Beam-Column-Joint" element proposed by Lowes et al. in OpenSEES, and the beams and columns were modeled using "Nonlinear-Beam-Column" elements with 2D fiber sections available in OpenSEES [10]. The effects of variables were investigated after the accuracy of model had been validated by comparing with the presented test data.

### 6.1. Modeling of normal concrete

The normal concrete was modeled using the "Concrete 02" material model [10] available in OpenSEES. The constitutive law of normal concrete, as shown in Fig. 10, was described using the model proposed by Giuffré–Pinto which was developed from Menegotto and Pinto [29], and the hysteretic rule for cyclic behavior of Concrete 02 was considered by stress-strain relationship

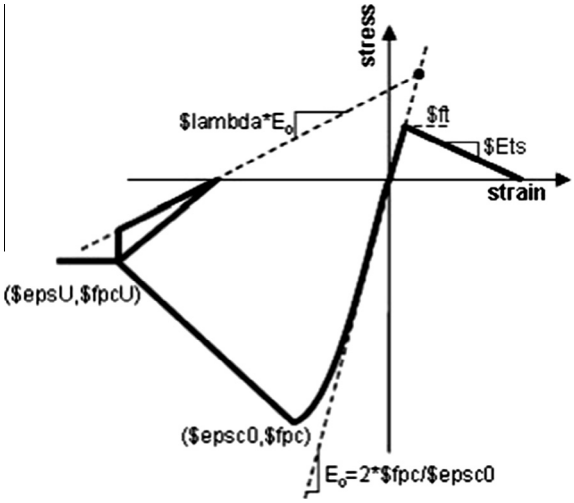


**Fig. 10.** Concrete 02 material—material parameters.

curve of normal concrete, as shown in Fig. 11. It unloads down to half of loading curve along with initial tangent stiffness, then unloads till tensile stress of concrete and reloads considering regression coefficients of stiffness. Its parameters in OpenSEES analysis were listed in Table 4 and values for concrete compressive properties were obtained from material tests associated with this study while others were calculated based on OpenSEES recommendations or current Chinese design guidance [5] as shown in the equations:

$$\varepsilon_0 = 2f'_c/E_0 \tag{2}$$

$$E_{ts} = 0.125E_0 \tag{3}$$

$$f_{pcu} = 0.2f'_c \tag{4}$$

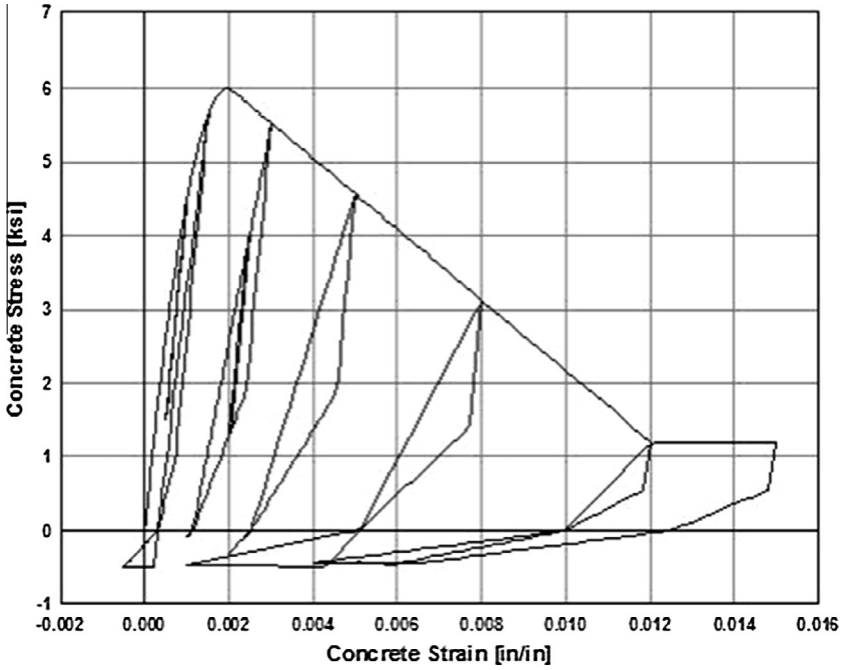


**Fig. 11.** Typical hysteretic stress-strain relation of concrete 02 model.

$$\varepsilon_{pcu} = 0.004 + 0.9\rho_{sv}(f_{yh}/300) \tag{5}$$

$$K = 1 + \frac{\rho_s f_{yh}}{f'_c} \tag{6}$$

and

$$f_t = 0.395 f_{cu}^{0.55} \tag{7}$$

where $\varepsilon_0$ is the strain at compressive strength; $f'_c$ is the cylinder compressive strength, $E_0$ is the elastic modulus of normal concrete/FRC, $E_{ts}$ is the tension softening stiffness, $f_{pcu}$ is the crushing strength of concrete/FRC, $\varepsilon_{pcu}$ is the crushing strain of concrete; $K$ is the constraint increasing coefficient caused by transverse reinforcements, $f_{yh}$ is the yield stress of transverse reinforcements, $f_{cu}$ represents the cubic compressive strength; and $f_t$ is the uniaxial tensile strength.

The mechanical properties of unconfined concrete can be applied to the mechanical properties of concrete confined within transverse reinforcements by multiplying constraint increasing coefficient $K$.

### 6.2. Modeling of FRC

The FRC was modeled using the "Concrete 02" material model as well in this study and its parameters used in OpenSEES are shown in Table 4. The compressive stress-strain relationship proposed by Li [30] was adopted to describe the uniaxial compressive behavior of FRC due to highly accuracy as Eq. (7).

$$y = \begin{cases} (Ax - x^2)/[1 + (A-2)x] & \text{if } 0 \leqslant x < 1 \\ (A_1 x)/[1 + (A_1 - 2)x + x^2] & \text{if } x \geqslant 1 \end{cases} \tag{8}$$

where $x = \varepsilon/\varepsilon_0$, $y = \sigma/\sigma_0$, $\sigma_0$ are the peak stress (uniaxial compressive strength in this study), $\sigma$ and $\varepsilon$ are the stress and corresponding strain of FRC at any time, $A_1$ is a parameter relating to the descending branch [30].

FRC exhibits strain-hardening behavior under uniaxial tension, so the uniaxial tensile behavior (Fig. 12) was described by using

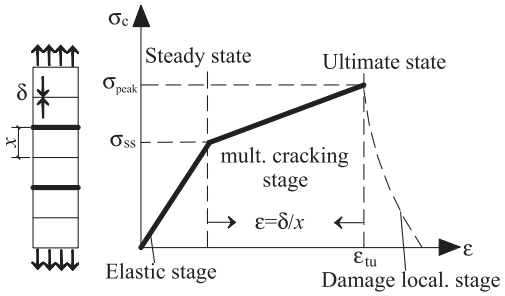


**Fig. 12.** Typical uniaxial tensile stress versus strain curve of FRC.

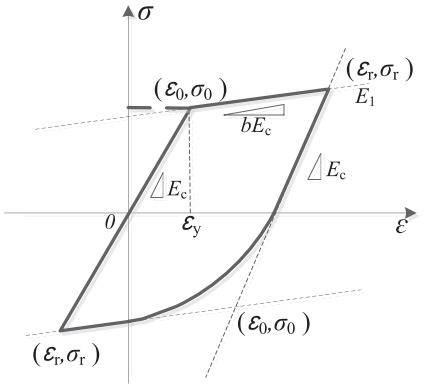


**Fig. 13.** The constative model of steel 02.

a bilinear strain hardening constitutive law proposed by Li [30] as Eq. (8).

$$\sigma_t = \begin{cases} E_0\varepsilon & \text{if } \varepsilon \leqslant \sigma_{ss}/E_0 \\ \sigma_i + E_{ie}\varepsilon & \text{if } \varepsilon > \sigma_{ss}/E_0 \end{cases} \tag{9}$$

where $\sigma_i = \sigma_{ss}(1 - E_{ie}/E_0)$, $\sigma_{ss}$ is the steady-state cracking stress defining the starting point of the hardening, $\sigma_{ss} = 0.896 f_t$, $E_{ie}$ is the tangential modulus of FRC in the multiple cracking stage.

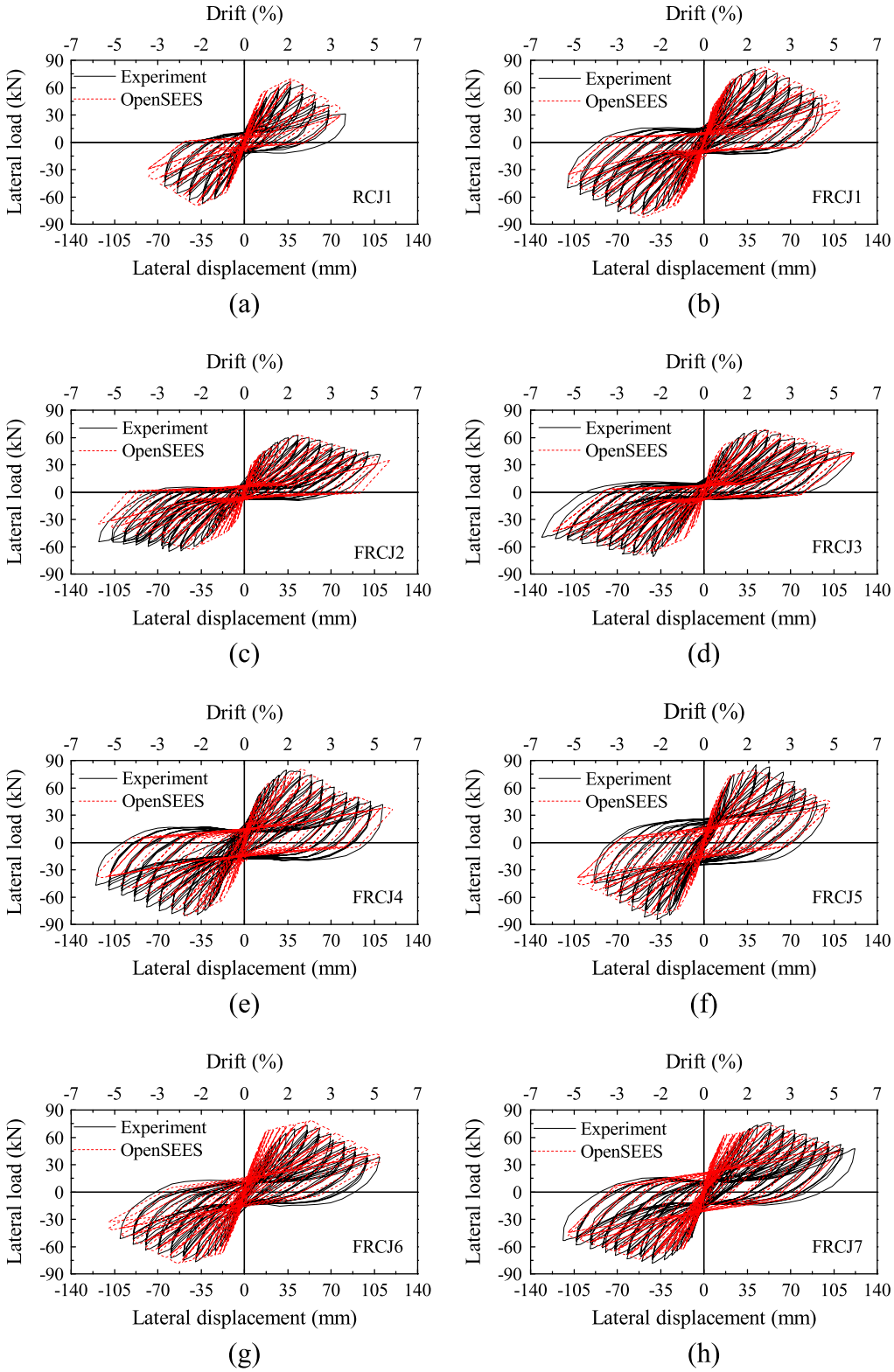


**Fig. 14.** Comparison of hysteretic curves of all specimens from experiment and numerical simulation.

Although the constitutive relationship of FRC is different from that of normal concrete, the calculation method of parameters used in OpenSEES is the same as the normal concrete except for the ultimate compressive strain of FRC. Based on uniaxial compressive test of FRC [30], the ultimate compressive strain of FRC is attained, which is listed in Table 4.

### 6.3. Modeling of steel reinforcement

The "Steel 02" material model, which is based on the Giuffré-Menegotto-Pinto model [29] revised by Fillipou et al. [31], available in OpenSEES was used to simulate the steel in the present models. The "Steel 02" material model in OpenSEES takes into

**Table 5**
Comparison between experimental value and simulation value of load-carrying capacity of all specimens at five feature points.

| Specimens | | Crack load point | | | Yield load point | | | Peak load point | | | Ultimate load point | | | Residual load point | | |
|---|---|---|---|---|---|---|---|---|---|---|---|---|---|---|---|---|
| | | $V_{jh,exp}$ | $V_{jh,sim}$ | $V_{jh,exp}/V_{jh,sim}$ | $V_{jh,exp}$ | $V_{jh,sim}$ | $V_{jh,exp}/V_{jh,sim}$ | $V_{jh,exp}$ | $V_{jh,sim}$ | $V_{jh,exp}/V_{jh,sim}$ | $V_{jh,exp}$ | $V_{jh,sim}$ | $V_{jh,exp}/V_{jh,sim}$ | $V_{jh,exp}$ | $V_{jh,sim}$ | $V_{jh,exp}/V_{jh,sim}$ |
| FRCJ1 | Push | 44.89 | 44.74 | 1.00 | 64.96 | 67.65 | 0.96 | 80.57 | 82.55 | 0.98 | 70.71 | 73.62 | 0.96 | 48.57 | 52.42 | 0.93 |
| | Pull | 50.07 | 48.65 | 1.03 | 64.78 | 67.63 | 0.96 | 79.27 | 82.56 | 0.96 | 70.49 | 73.64 | 0.96 | 50.26 | 52.44 | 0.96 |
| FRCJ2 | Push | 34.67 | 35.65 | 0.97 | 49.97 | 52.67 | 0.95 | 61.95 | 62.99 | 0.98 | 52.63 | 51.73 | 1.02 | 41.44 | 39.18 | 1.06 |
| | Pull | 34.79 | 35.17 | 0.99 | 49.91 | 52.67 | 0.95 | 64.25 | 63.00 | 1.02 | 59.70 | 51.74 | 1.15 | 54.39 | 39.19 | 1.39 |
| FRCJ3 | Push | 35.00 | 40.20 | 0.87 | 54.97 | 55.47 | 0.99 | 68.38 | 68.76 | 0.99 | 58.89 | 63.08 | 0.93 | 43.69 | 43.50 | 1.00 |
| | Pull | 39.79 | 39.78 | 1.00 | 55.06 | 55.46 | 0.99 | 71.15 | 68.75 | 1.03 | 63.13 | 59.22 | 1.07 | 49.46 | 47.45 | 1.04 |
| FRCJ4 | Push | 45.42 | 44.73 | 1.02 | 59.78 | 63.69 | 0.94 | 78.54 | 80.63 | 0.98 | 68.71 | 64.42 | 1.07 | 41.63 | 49.96 | 0.83 |
| | Pull | 44.87 | 44.75 | 1.00 | 59.79 | 63.70 | 0.94 | −80.61 | 80.62 | 0.99 | 75.19 | 64.43 | 1.17 | 46.86 | 38.50 | 1.22 |
| FRCJ5 | Push | 60.02 | 59.33 | 1.01 | 74.77 | 73.03 | 1.02 | 84.96 | 79.60 | 1.07 | 67.24 | 65.44 | 1.03 | 50.18 | 46.68 | 1.08 |
| | Pull | 59.74 | 59.39 | 1.01 | 74.52 | 73.04 | 1.02 | 84.75 | 79.60 | 1.06 | 66.84 | 65.45 | 1.02 | 45.08 | 46.69 | 0.97 |
| FRCJ6 | Push | 39.80 | 42.25 | 0.94 | 59.40 | 65.08 | 0.91 | 72.93 | 78.55 | 0.93 | 63.41 | 67.57 | 0.94 | 37.70 | 41.56 | 0.91 |
| | Pull | 54.49 | 43.69 | 1.25 | 59.71 | 65.08 | 0.92 | 76.66 | 78.39 | 0.98 | 72.31 | 72.38 | 1.00 | 51.34 | 41.55 | 1.24 |
| FRCJ7 | Push | 44.92 | 42.84 | 1.05 | 65.17 | 63.38 | 1.03 | 75.94 | 73.99 | 1.03 | 63.42 | 64.85 | 0.98 | 47.56 | 50.32 | 0.95 |
| | Pull | 54.53 | 42.58 | 1.28 | 65.02 | 63.52 | 1.02 | 78.36 | 73.99 | 1.06 | 69.59 | 64.85 | 1.07 | 53.63 | 50.32 | 1.07 |
| RCJ1 | Push | 49.83 | 41.90 | 1.19 | 59.49 | 57.15 | 1.04 | 66.33 | 70.09 | 0.95 | 52.38 | 59.85 | 0.88 | 31.19 | 41.15 | 0.76 |
| | Pull | 49.05 | 41.77 | 1.17 | 62.35 | 57.14 | 1.09 | 67.82 | 70.14 | 0.97 | 55.95 | 59.78 | 0.94 | 48.37 | 41.16 | 1.18 |

*Note:* $V_{jh,exp}$ and $V_{jh,sim}$ represent the experimental and simulation load-carrying capacity, respectively.

**Table 6**
Comparison between experimental value and simulation value of lateral drift of all specimens at five feature points.

| Specimens | | Crack load point | | | Yield load point | | | Peak load point | | | Ultimate load point | | | Residual load point | | |
|---|---|---|---|---|---|---|---|---|---|---|---|---|---|---|---|---|
| | | $\theta_{jh,exp}$ | $\theta_{jh,sim}$ | $\theta_{jh,exp}/\theta_{jh,sim}$ | $\theta_{jh,exp}$ | $\theta_{jh,sim}$ | $\theta_{jh,exp}/\theta_{jh,sim}$ | $\theta_{jh,exp}$ | $\theta_{jh,sim}$ | $\theta_{jh,exp}/\theta_{jh,sim}$ | $\theta_{jh,exp}$ | $\theta_{jh,sim}$ | $\theta_{jh,exp}/\theta_{jh,sim}$ | $\theta_{jh,exp}$ | $\theta_{jh,sim}$ | $\theta_{jh,exp}/\theta_{jh,sim}$ |
| FRCJ1 | Push | 0.006 | 0.005 | 1.23 | 0.010 | 0.010 | 1.02 | 0.020 | 0.023 | 0.84 | 0.033 | 0.030 | 1.10 | 0.045 | 0.046 | 0.83 |
| | Pull | 0.009 | 0.006 | 1.55 | 0.014 | 0.010 | 1.33 | 0.023 | 0.023 | 1.00 | 0.038 | 0.030 | 1.26 | 0.052 | 0.046 | 0.95 |
| FRCJ2 | Push | 0.005 | 0.004 | 1.25 | 0.010 | 0.013 | 0.81 | 0.021 | 0.020 | 1.02 | 0.034 | 0.035 | 0.98 | 0.051 | 0.051 | 0.84 |
| | Pull | 0.010 | 0.004 | 2.28 | 0.014 | 0.013 | 1.10 | 0.024 | 0.020 | 1.20 | 0.037 | 0.035 | 1.07 | 0.056 | 0.051 | 0.93 |
| FRCJ3 | Push | 0.005 | 0.005 | 1.05 | 0.011 | 0.011 | 1.01 | 0.020 | 0.023 | 0.86 | 0.035 | 0.031 | 1.11 | 0.055 | 0.058 | 0.88 |
| | Pull | 0.009 | 0.005 | 1.87 | 0.014 | 0.011 | 1.29 | 0.020 | 0.023 | 0.84 | 0.036 | 0.037 | 0.99 | 0.062 | 0.053 | 0.99 |
| FRCJ4 | Push | 0.005 | 0.005 | 1.00 | 0.008 | 0.009 | 0.93 | 0.019 | 0.022 | 0.85 | 0.030 | 0.031 | 0.96 | 0.053 | 0.043 | 0.86 |
| | Pull | 0.009 | 0.005 | 1.93 | 0.011 | 0.009 | 1.25 | 0.023 | 0.022 | 1.06 | 0.033 | 0.031 | 1.04 | 0.057 | 0.055 | 0.92 |
| FRCJ5 | Push | 0.008 | 0.007 | 1.15 | 0.011 | 0.010 | 1.18 | 0.020 | 0.019 | 1.04 | 0.035 | 0.031 | 1.12 | 0.043 | 0.047 | 0.85 |
| | Pull | 0.009 | 0.007 | 1.33 | 0.014 | 0.010 | 1.42 | 0.018 | 0.019 | 0.94 | 0.032 | 0.031 | 1.04 | 0.042 | 0.047 | 0.83 |
| FRCJ6 | Push | 0.008 | 0.005 | 1.81 | 0.014 | 0.008 | 1.70 | 0.024 | 0.025 | 0.95 | 0.033 | 0.033 | 1.00 | 0.052 | 0.051 | 0.94 |
| | Pull | 0.008 | 0.005 | 1.60 | 0.009 | 0.008 | 1.13 | 0.019 | 0.025 | 0.74 | 0.028 | 0.030 | 0.94 | 0.048 | 0.051 | 0.87 |
| FRCJ7 | Push | 0.009 | 0.005 | 2.00 | 0.015 | 0.009 | 1.72 | 0.025 | 0.025 | 1.01 | 0.039 | 0.034 | 1.14 | 0.058 | 0.050 | 0.98 |
| | Pull | 0.006 | 0.005 | 1.34 | 0.010 | 0.012 | 0.88 | 0.020 | 0.025 | 0.80 | 0.034 | 0.034 | 0.99 | 0.054 | 0.050 | 0.87 |
| RCJ1 | Push | 0.008 | 0.005 | 1.78 | 0.013 | 0.009 | 1.54 | 0.018 | 0.018 | 0.98 | 0.027 | 0.024 | 1.13 | 0.033 | 0.035 | 0.86 |
| | Pull | 0.006 | 0.005 | 1.36 | 0.012 | 0.009 | 1.36 | 0.016 | 0.018 | 0.90 | 0.026 | 0.024 | 1.08 | 0.031 | 0.035 | 0.81 |

*Note:* $\theta_{jh,exp}$ and $\theta_{jh,sim}$ represent the experimental and simulation lateral drift of column top, respectively.

account isotropic strain hardening rule and Bauschinger effect [32] shown in Fig. 13. The critical parameters involved in the model were introduced in Section 4.2.3. This material model is detailed in the relevant literature such as Elmorsi [33].

The control parameters $R0, $cR1, $cR2 transiting from elastic to plastic branches, which reflects the Bauschinger effect, is 18.5, 0.925 and 0.15, respectively. The isotropic hardening parameters $a1, $a2, $a3 and $a4 is 0, 1, 0 and 1, respectively.

### 6.4. Modeling verification

Fig. 14 demonstrates the comparison of hysteretic curves of all specimens from experiment and numerical simulation. Both the pinching effect and hysteretic loops were accurately captured by the proposed FE models. It can be seen from Tables 5 and 6 that the mean ratios of experimental value to simulation value of load-carrying capacity at crack load point, yield load point, peak load point, ultimate load point and residual load point is 1.05, 0.99, 1.00, 1.02 and 1.05, and the corresponding coefficients of variations are 0.30, 0.27, 0.27, 0.27 and 0.28, respectively, indicating that the results predicted by the proposed FE models are in good agreement with the test data. It can be also that the mean ratios of experimental value to simulation value of lateral drift at crack load point, yield load point, peak load point, ultimate load point and residual load point is 1.55, 1.24, 0.94, 1.04 and 0.89, and the corresponding coefficients of variations are 0.20, 0.22, 0.26, 0.24 and 0.30, respectively. Although the mean ratio of experimental value to simulation value of lateral drift is a little large, the numerical simulated results can be used to predict the actual deformation capability of FRC beam-column joints.

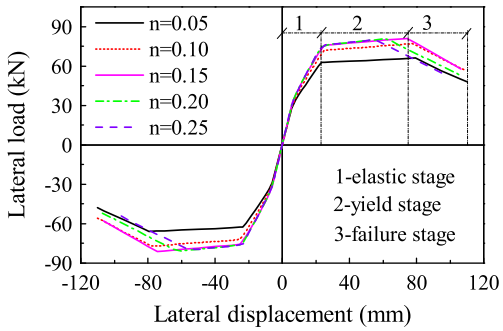


**Fig. 15.** Skeleton curves with different axial load ratios.

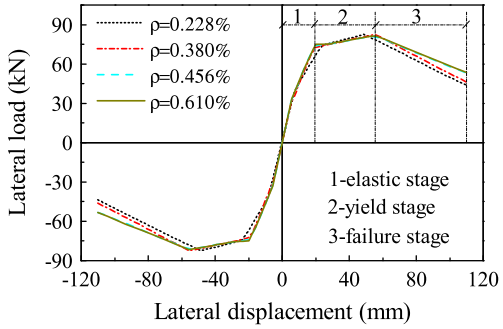


**Fig. 16.** Skeleton curves with different transverse reinforcement ratios in the joint core zone.

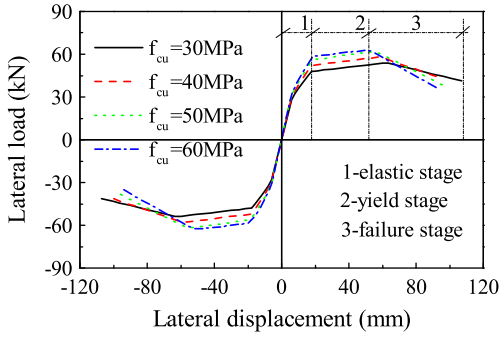


**Fig. 17.** Skeleton curves with different FRC compressive strength.

## 7. Parametrical study

In order to deeply understand the seismic performance of the FRC specimens, a parametric study was then conducted with the help of the proposed FE models.

### 7.1. Effects of axial load ratio

The skeleton curves obtained from the proposed models corresponding to the axial load ratio varying from 0.05 to 0.25 with 0.05 intervals are shown in Fig. 15. All skeleton curves can be simply described using a trilinear relationship including an elastic stage, a yield stage and a failure stage. It is found that the increase of axial load ratio leads to a slight increases in the initial tangent stiffness in the elastic stage. A greater axial load ratio delivers an earlier occurrence of failure corresponding to a shorter length of yield stage. A greater axial load ratio results in an increment in the load-carrying capacity which was evident from the experimental results as well. The post-peak deterioration of the FRC specimens during the failure stage is accelerated due to an increase in the axial load ratio being verified by a more brittle failure stage.

### 7.2. Effects of transverse reinforcement ratio in the joint core zone

The skeleton curves from different transverse reinforcement ratios of 0.228, 0.380, 0.456% and 0.610% in the joint core zone are shown in Fig. 16. As transverse reinforcement ratios of the joint core zone increases, the initial tangent stiffness is still almost similar. However, a greater transverse reinforcement ratio postpones the occurrence of failure and promotes the deformation capability. Meanwhile, it shows a negligible effect on the skeleton curves until the transverse reinforcement ratio enlarges to a certain level such as 0.456% in the current study. It may imply that the FRC can effectively reduce the usage of transverse reinforcements and consequently diminish the complexity of construction.

### 7.3. Effects of FRC compressive strength

Fig. 17 shows the results of skeleton curves corresponding to the FRC cubic compressive strength of 30, 40, 50 and 60 MPa in the joint core zone. An increment of FRC compressive strength leads to a slight improvement in the initial tangent stiffness. It is clearly that a higher strength of FRC can dramatically promote the load-carrying capacity while the deformation capability of beam-column joints will be lower. However, this improvement almost terminates as long as the strength is greater than a certain level, such as 50 MPa adopted in the present study.

## 8. Conclusions

This paper presents a combination of experimental and numerical study on the application of FRC to replace the normal concrete casted in beam-column joints in order to improve seismic performance. The findings from the presented well-conducted experimental study has proved that FRC as an advanced alternative can effectively promote the seismic performance of beam-column joints. The proposed experimental study consisted of eight beam-column joints and investigated the influences on the seismic performances from the different axial load ratios and transverse reinforcement ratios of the joint core zone. An effective numerical model was conducted to furtherly investigate the influences from critical parameters after its accuracy was validated. The key conclusions can be drawn as follows.

(1) Compared with the RC specimen, there were more multiple diagonal cracks occurred in FRC specimens. It can be contributed to its multiple cracking behavior as the consequence of excellent bridging capacity donated by PVA fiber. In the view of failure modes, using of FRC can effectively restrain the crack widening and eliminate the damages caused by the spalling of concrete cover.
(2) The increment of transverse reinforcement ratio in the joint core zone experienced an improvement in the ultimate deformation capability although it has negligible effects on the load-carrying capacity. It may imply that it is possible to decrease the usage of transverse reinforcements with benefits of controlling construction cost and eliminating the member congestion without deleteriously affecting the seismic performance of the structures.
(3) Plastic hinges formed in the column close to the beam faces when the flexural strength ratio of column to beam was <1, otherwise the plastic hinge formed in the beams close to the column faces. The increment of axial load ratio can promote the seismic performance of beam-column joints by

improving the load-carrying capacity and energy dissipation capacity. As expected, a higher compressive strength of FRC can dramatically improve the load-carrying capacity of beam-column joints while the deformation capability will be reduced.

## Acknowledgements

The author gratefully acknowledges the funding supported by the National Natural Science Foundation of China (Grant No. 51278402).

## Appendix A. Supplementary material

Supplementary data associated with this article can be found, in the online version, at http://dx.doi.org/10.1016/j.engstruct.2016.08.001.

## References

[1] Hassan W, Park S, Lopez R, Mosalam K, Moehle J. Seismic response of older-type reinforced concrete corner joints. In: Proc 9th US National and 10th Canadian conference on earthquake engineering: reaching beyond borders, Toronto, Canada, July 25–29.
[2] Ong K, Lin ZS, Chandra LR, Tam CT, Pang SD. Experimental investigation of a DfD moment-resisting beam–column connection. Eng Struct 2013;56:1676–83.
[3] Guo ZX, Yang Y. Experimental study on the deformation characteristics of RC beam-column subassemblages. Struct Eng Mech 2005;21(4):393–406.
[4] ACI-ASCE Committee 352. Recommendations for design of beam-column connections in monolithic reinforced concrete structures. ACI 352R-02. Farmington Hills, Michigan: American Concrete Institute; 2002.
[5] GB 50010-2010. Code for design of concrete structures. Beijing: China Building Press; 2011.
[6] Fantilli AP, Mihashi H, Vallini P. Multiple cracking and strain hardening in fiber-reinforced concrete under uniaxial tension. Cem Concr Res 2009;39(12):1217–29.
[7] Li VC, Wang S, Wu C. Tensile strain-hardening behavior of polyvinyl alcohol engineered cementitious composite (PVA-ECC). ACI Mater J 2001;98(6):483–92.
[8] Parra-Montesinos GJ. High-performance fiber-reinforced cement composites: an alternative for seismic design of structures. ACI Struct J 2005;102(5):668–75.
[9] Canbolat BA, Parra-Montesinos GJ, Wight JK. Experimental study on seismic behavior of high-performance fiber-reinforced cement composite coupling beams. ACI Struct J 2005;102(1):159–66.
[10] Open system for earthquake engineering simulation (OpenSEES). <http://opensees.berkeley.edu/>.
[11] Wang YJ, Liang XW, Wu JW. Calculation model of shear capacity of fiber-reinforced concrete beam-column joint. Eng Mech 2016;33(3):77–86 [in Chinese].
[12] Wang YJ, Liang XW. Calculation of the shear capacity of fiber-reinforced concrete beam-column joint. Eng Mech 2015;32(12):161–7 [in Chinese].
[13] Henager CH. Steel fibrous, ductile concrete joint for seismic-resistant structures. Reinforced concrete in seismic zones, SP-53. Detroit: American Concrete Institute; 1977. p. 371–86.
[14] Filiatrault A, Ladicani K, Massicotte B. Seismic performance of code-designed fiber-reinforced concrete joints. ACI Struct J 1994;91(5):564–71.
[15] Parra-Montesinos GJ, Peterfreund SW, Chao S-H. Highly damage-tolerant beam-column joints through use of high-performance fiber-reinforced cement composites. ACI Struct J 2005;102(3):487–95.
[16] Qudah S, Maalej M. Application of engineered cementitious composites (ECC) in interior beam–column connections for enhanced seismic resistance. Eng Struct 2014;69:235–45.
[17] Gefken PR, Ramey MR. Increased joint hoop spacing in type 2 seismic joints using fibre reinforced concrete. ACI Struct J 1989;86(2):168–72.
[18] Bayasi Z, Gebman M. Reduction of lateral reinforcement in seismic beam-column connection via application of steel fibers. ACI Struct J 2002;99(6):772–80.
[19] Shannag MJ, Barakat S, Abdul KareemM. Cyclic behavior of HPFRC repaired interior beam column joints. Mater Struct 2002;35(6):348–56.
[20] Shannag MJ, Abu-Dyya Nabeela, Abu-Farsakh Ghazi. Lateral load response of high performance fiber reinforced concrete beam–column joints. Constr Build Mater 2005;19(9):500–8.
[21] Shannag MJ, Abu-Farsakh G, Abu-Dyya N. Modeling the cyclic response of fiber reinforced concrete joints. Eng Struct 2007;29(11):2960–7.
[22] Zhang Y, Harries KA, Yuan WC. Experimental and numerical investigation of the seismic performance of hollow rectangular bridge piers constructed with and without steel fiber reinforced concrete. Eng Struct 2013;48(3):255–65.
[23] Bedirhanoglu I, Ilki A, Kumbasar N. Precast fiber reinforced cementitious composites for seismic retrofit of deficient RC joints – a pilot study. Eng Struct 2013;52(6):192–206.
[24] Abbas AA, Mohsin SMS, Cotsovos DM. Seismic response of steel fibre reinforced concrete beam–column joints. Eng Struct 2014;59(2):261–83.
[25] Said SH, Razak HA. Structural behavior of RC engineered cementitious composite (ECC) exterior beam–column joints under reversed cyclic loading. Constr Build Mater 2016;107(1):226–34.
[26] Gao SL. Study on pseudo strain-hardening and fracture characteristic of polyvinyl alcohol fiber reinforced cementitious composites PhD thesis. Dalian: Dalian University of Technology; 2006.
[27] Zhu BL. Seismic test of building structures. Beijing: Earthquake Press; 2003.
[28] JGJ/T 101-2015. Specification for seismic test of buildings. Beijing: China Architecture & Building Press; 2015.
[29] Menegotto M, Pinto P. Method of analysis for cyclically loaded RC plane frames including changes in geometry and non-elastic behavior of elements under combined normal force and bending. In: IABSE symposium: resistance and ultimate deformability of structures acted on by well-defined repeated loads, final report, Lisbon (Portugal).
[30] Li Y. Study on mechanical performance of high performance fiber reinforced cement composite PhD thesis. Xi'an University of Architecture and Technology; 2011 [in Chinese].
[31] Fillipou FC, Popov EP, Bertero VV. Effects of bond deterioration on hysteretic behavior of reinforced concrete joints. EERC report no. UCB/EERC-83/19; August 1983.
[32] Mazzoni S, McKenna F, Scott MH, Fenves GL. OpenSees command language manual. Berkeley (USA): Pacific Earthquake Engineering Research Center, University of California; 2007.
[33] Elmorsi SEM. Analytical modeling of reinforced concrete beam column connections for seismic loading Open access dissertations and theses. McMaster University; 1998.